Physica Scripta

PAPER • **OPEN ACCESS**

Anomalous magnetoresistance around the critical temperature in heterostructures of high-T_c superconducting $YBa_2Cu_3O_{7-x}$ and ferromagnetic $SrRuO_3$ with perpendicular magnetic anisotropy

To cite this article: V A de Oliveira Lima *et al* 2025 *Phys. Scr.* **100** 075985

Physica Scripta

PAPER

Anomalous magnetoresistance around the critical temperature in heterostructures of high-T_c superconducting $YBa_2Cu_3O_{7-x}$ and ferromagnetic $SrRuO_3$ with perpendicular magnetic anisotropy

V A de Oliveira Lima[1,2,*], M I Faley[3], O Concepción[4], S Nandi[1,2], P Prakash[1], M H Hamed[1,5], E Kentzinger[1], T Brückel[1,2] and C Bednarski-Meinke[1]

[1] Jülich Centre for Neutron Science for Quantum Materials and Collective Phenomena (JCNS-2), Forschungszentrum Jülich GmbH, 52425 Jülich, Germany
[2] RWTH Aachen University, 52074 Aachen, Germany
[3] Ernst Ruska-Centre for Microscopy and Spectroscopy with Electrons (ER-C-1), Forschungszentrum Jülich GmbH, 52425 Jülich, Germany
[4] Peter Grünberg Institute for Semiconductor Nanoelectronics (PGI-9), Forschungszentrum Jülich GmbH, 52425 Jülich, Germany
[5] Faculty of Science, Helwan University, 11795 Cairo, Egypt
[*] Author to whom any correspondence should be addressed.

E-mail: v.de.oliveira.lima@fz-juelich.de

Keywords: proximity effect, anisotropic coherence length, magnetic anisotropy, magnetotransport, superconductivity, magnetism, surface and interfacial phenomena

Supplementary material for this article is available online

OPEN ACCESS

RECEIVED
24 January 2025

REVISED
25 February 2025

ACCEPTED FOR PUBLICATION
24 June 2025

PUBLISHED
4 July 2025

Abstract

Heterostructures based on superconductors and ferromagnets show strong potential for innovating device applications in spintronics and quantum computing. $SrRuO_3$ (SRO) has recently attracted much attention among transition metal oxides because it is the only 4*d* oxide to exhibit itinerant ferromagnetism and metallic conductivity. $YBa_2Cu_3O_{7-x}$ (YBCO) is one of the most studied high critical temperature (high-T_c) superconductors with a wide range of potential applications. We report morphological, structural, magnetic and magnetotransport characterization of YBCO/SRO (HS-YS) and SRO/YBCO (HS-SY) heterostructures grown on low miscut $SrTiO_3$ (001) single crystals by high oxygen pressure sputtering. All samples exhibit epitaxial growth with good crystal quality and sharp interfaces. The heterostructures exhibit T_c of 87 K and 57 K for HS-YS and HS-SY, respectively, both reduced compared to bulk YBCO (91 K). The reduction in T_c and intriguing features in magnetoresistance measurements around the onset of superconductivity are robust indicators that a proximity effect takes place in such heterostructures, and inspire further theoretical and experimental investigations.

1. Introduction

Proximity effects are intriguing phenomena that emerge from the interfaces of thin film heterostructures. Of particular interest are such effects at interfaces between superconductors and ferromagnets, due to the intrinsically strong electron correlation effects in these classes of materials [1]. Such phenomena originate from the competition between the superconducting (SC) and ferromagnetic (FM) electronic structures. They have been studied theoretically and experimentally [2–4]. The potential exploitation of proximity effects in superconducting spintronics [5], in the development of fluxonic devices [6, 7] for quantum computing and in the development of quantum electronics [8], has motivated their more detailed study.

Recent magnetotransport and neutron scattering experiments on Nb/FePd heterostructures have revealed proximity effects associated with the strength of the perpendicular magnetic anisotropy (PMA) of the FM layer [9–11]. Domain-wall and reverse domain superconductivity were observed in heterostructures with FePd layer showing high PMA and maze magnetic domain structure, whereas long-range supercurrents through the FePd

layer were observed in heterostructures with low PMA and stripe magnetic domain structure. These results demonstrate that it is possible to control the superconducting order parameter at the nanoscale by adjusting the PMA. Important to note is that these proximity effects appear due to the comparable energy and length scales: on the one hand the comparable magnitudes of the FM stray-fields and the second critical field (B_{c2}) of the SC, and on the other hand, the generation of spin-triplet Cooper pairs with large penetration length into the FM compatible with the typical dimensions of the in-plane magnetic texture of the FM layer [4, 12–14]. Typical proximity effects in the form of oscillations of the critical temperature (T_c) and diverging magnetoresistance are observed when the thickness of the FM layer is varied in FM/SC/FM and multilayer heterostructures based on conventional SC and FM metals and metallic alloys [15, 16].

Unique proximity effects are observed in SC/FM thin film heterostructures based on high-T_c SC and FM spin-valves, which generally show in-plane magnetic anisotropy [17], such as $YBa_2Cu_3O_{7-x}$ (YBCO)/$La_{1-x}Ca_xMnO_3$ (LCMO) and YBCO/$La_{1-x}Sr_xMnO_3$ (LCMO). In such heterostructures, a magnetic proximity effect is observed above T_c, where a magnetic dead or depleted layer forms at the SC/FM interface and suppresses the magnetic moment in the FM layer [3]. Below T_c, a superconducting proximity effect occurs. Spin-triplet Cooper pairs leak into the FM-layer resulting in a subsequent decrease in T_c. In oxide multilayers and tunnel-junctions with uniform magnetization, it has been observed that the FM layers can align antiferromagnetically, resulting in the induction of a small magnetic moment into the SC via charge-transfer driven by orbital ordering, and giant magnetoresistance [18–21]. Additionally, spin-triplet characteristics have been detected in SC/FM planar devices utilizing high-T_c SC with FM junctions exhibiting in-plane magnetization. The decay of supercurrents at distances around a few micrometers and the modulation of the magnetoresistance signal, with an oscillation periodicity of $\approx$ 30 mT, as well as the increase of in-plane supercurrents when the Cu orbital moment is aligned perpendicular to the magnetization of the FM layer suggests that spin-triplet Cooper pairs are present and are responsible for a long-range proximity effect [22, 23]. Long-range spin-triplet correlations have also been reported in SC/FM thin film heterostructures with noncollinear magnetization. In such systems, the noncollinear magnetization arises from two FM oxide layers, where one exhibits PMA and the other exhibits in-plane magnetic anisotropy. Superconducting currents were observed up to a total heterostructure thickness of 50 nm, related to spin-polarized (spin-triplet) Cooper pairs generated by the noncollinear magnetization of the FM layers in the heterostructure [24–26]. Although many results have been reported on proximity effects in heterostructures based on high-T_c SC and FM materials with in-plane magnetic anisotropy, a detailed study is still lacking when considering proximity effects of high-T_c SC with FM exhibiting PMA.

Recently, $SrRuO_3$ (SRO) has attracted considerable interest as a promising material in the emerging field of quantum electronics, a novel form of electronics based on the quantum degrees of freedom [8]. This new application of SRO would move it beyond consideration as only an electrode in ferroelectric capacitors and superconducting junctions [27, 28]. SRO is the only one 4*d* oxide that presents both itinerant ferromagnetism and metallic conductivity below $T_{Curie} = 160$ K, and also exhibits strong PMA when epitaxially grown on $SrTiO_3$ (STO) substrates [8, 29]. Moreover, it shows high spin–orbit coupling as well as anomalous Hall and Berry effects, desirable properties for developing Berrytronics and topological superconductivity [8, 30–34]. The structural compatibility and subsequent interplay of physical properties between SRO and other technologically relevant oxides are being explored, paving the way for applications in various fields such as electronics, catalysis, energy storage, and more [35]. In the present context, the SRO narrow domain wall width of 3 nm, with magnetic periodicity ranging from 200 nm to 1 μm [36], which is suitable for the generation of spin-triplet states, has motivated a more detailed study of its interfacial proximity effects with high-T_c superconductors. A highly localized long-range proximity effect has been observed in a bilayer heterostructure of SRO/YBCO [37]. Low-temperature scanning tunneling microscopy revealed that crossed Andreev reflections around well-defined stripe regions near domain walls are responsible for the penetration of the SC order parameter into the SRO layer to depths up to 20 nm.

STO is considered the standard substrate for the epitaxial growth of many complex oxides, such as SRO, because above 105 K it has cubic perovskite crystal structure with a lattice parameter of 3.905 Å [38, 39]. SRO, on the other hand, has an orthorhombic crystal structure (space group *Pbnm*) with lattice parameters of $a_{or} = 5.53$ Å, $b_{or} = 5.57$ Å and $c_{or} = 7.85$ Å [8, 40]. Since SRO has an aristotype perovskite structure, its orthorhombic unit cell comprises four units derived from the perfect cubic perovskite structure. This arrangement leads to a pseudocubic lattice constant $a_{pc} = 3.93$ Å [8, 40, 41], which is quite compatible with STO substrate. YBCO has an orthorhombic crystal structure (space group *Pmmm*) with lattice parameters of $a = 3.8227$ Å, $b = 3.8872$ Å and $c = 11.6802$ Å [42]. Therefore, epitaxial growth is possible given the lattice mismatch of 0.64% for SRO/STO, 1.66% for YBCO/STO and ~2% for YBCO/SRO [43].

We report on the growth and characterization of YBCO/SRO and SRO/YBCO thin film heterostructures, with the aim to investigate proximity effects in high-T_c SC coupled with FM with PMA. The coexistence of SC and FM together with the reduction of T_c and anomalous magnetoresistance near the SC onset suggest that a

proximity effect occurs at the YBCO/SRO interface. This effect may be driven by the competition of the SC and FM anisotropies and inspires further investigation.

2. Experimental details

$SrTiO_3$ (001) single crystals with miscut angle between 0.05° and 0.1° were used as substrates as they provide the most suitable surface for the coherent growth of SRO films while ensuring the presence of PMA [29]. Prior to growth, the substrates were chemically etched for 30 s using a buffered NH_4F-HF (BHF) solution and then annealed at 950 °C for 2 h in air to obtain a well defined TiO_2 surface termination [44].

The thin films and heterostructures described in this work were prepared from stoichiometric SRO and YBCO targets using High Oxygen Pressure Sputtering (HOPS) [45–47]. Prior to deposition, a base pressure of 10^{-6} mbar is stabilized and the targets are pre-sputtered for one day to ensure a clean deposition chamber and a target free of contaminants. Pure oxygen (99.99%) is used as a process gas and pressures (PO_2) in the range of 1 to 3 mbar are achieved by the combination of mass flow controller, oil-free backing pump and turbomolecular pump. The substrates are placed directly on a heater block. We define the temperature of the heater block as the growth temperature (T_{dep}). The target-substrate distance (D_{TS}) ranges between 1 and 3.5 cm. D_{TS} directly correlates to growth rate and surface quality, and has been separately optimized for both SRO and YBCO. The targets can be sputtered using two different methods of plasma generation, Radio frequency (RF) and Direct Current (DC).

SRO layers were deposited using RF sputtering at $T_{dep} = 785$ °C, $PO_2 = 1.5$ mbar and $D_{TS} = 2.5$ cm in a HOPS system dedicated to the growth of transition metal oxide films. YBCO layers were deposited using DC sputtering at $T_{dep} = 930$ °C, $PO_2 = 2.5$ mbar and $D_{TS} = 1$ cm in a separate dedicated HOPS system. Precise pyrometer measurements of the substrate temperature show that it is about 110 °C lower than T_{dep}. This is in agreement with [48]. SRO has a growth rate of 12.5 nm/h, while YBCO has a growth rate of 100 nm/h. To achieve the correct oxygen vacancy concentration in YBCO and ensure the highest possible T_c, a post-annealing treatment was carried out by cooling the YBCO to 500 °C and holding it at this temperature at a pressure of 10 mbar for 24 hours [49, 50]. Heterostructures of YBCO/SRO (HS-YS) and SRO/YBCO (HS-SY) were prepared by a two-step process that combines the above described deposition of SRO and YBCO. Heterostructure HS-SY was subjected to two post-annealing processes: one after YBCO growth and another after SRO growth. The second annealing time was 30 min. This is performed to assure a high critical temperature in the heterostructure, as during the high oxygen pressure growth of SRO the oxygen content in YBCO is reduced and recovers much more slowly during a second annealing due to the limited diffusion of oxygen through the SRO layer.

Sample morphology and local roughness were characterized by Atomic Force Microscopy (AFM) using an Agilent 5400 AFM/SPM microscope in intermittent contact mode with Mikromash type HQ:NSC15 cantilevers. The crystal structure, layer thickness and total roughness were investigated by means of X-ray diffraction (XRD) and X-ray reflectivity (XRR) measurements performed on a Rigaku SmartLab diffractometer. The epitaxial growth and the atomic scale structure were probed by cross-sectional high-resolution transmission electron microscopy (HR-TEM) on a FEI Titan G2 60-300 HOLO microscope and a FEI Titan 80-300 TEM. Magnetic hysteresis, zero-field cooled and field cooled measurements were performed to investigate the magnetic field and temperature dependence of the magnetization. The measurements were carried out on a Superconducting Quantum Interference Device (SQUID) MPMS-XL Magnetometer and on a Physical Properties Measurement System (PPMS DynaCool) with the Vibrating Sample Magnetometer (VSM) option. Temperature dependence of the electrical transport and magnetotransport measurements were performed using the standard four-point probe method on a Physical Properties Measurement System (PPMS) from Quantum Design. Sample stoichiometry was characterized by Rutherford Backscattering Spectroscopy (RBS).

3. Characterization and results

3.1. Morphology and structural characterization

Post-etched and annealed STO substrates exhibited a TiO_2 surface termination, characterized by a terraced morphology of one STO unit cell in height. A schematic representation of the SRO thin film, HS-YS and HS-SY are depicted in figures 1(a), (b) and (c), respectively. The thicknesses of the SRO thin film and the HS-YS and HS-SY heterostructures were measured using X-ray reflectivity and cross-sectional TEM (see Supplementary Material [51], figures S1 and S2). The morphology of the YBCO thin films has been extensively studied and is reported elsewhere [52, 53]. The AFM topography and phase micrographs of all prepared samples are shown in figures 1(d)–(i). The SRO thin film exhibits a smooth surface with local root mean square roughness $\sigma < 1$ nm. A terraced termination mimicking the TiO_2 termination of the STO substrate can be observed in figure 1(d). The homogeneity of the SRO thin film can be observed across the 5 x 5 μm^2 scan area of the phase micrograph shown

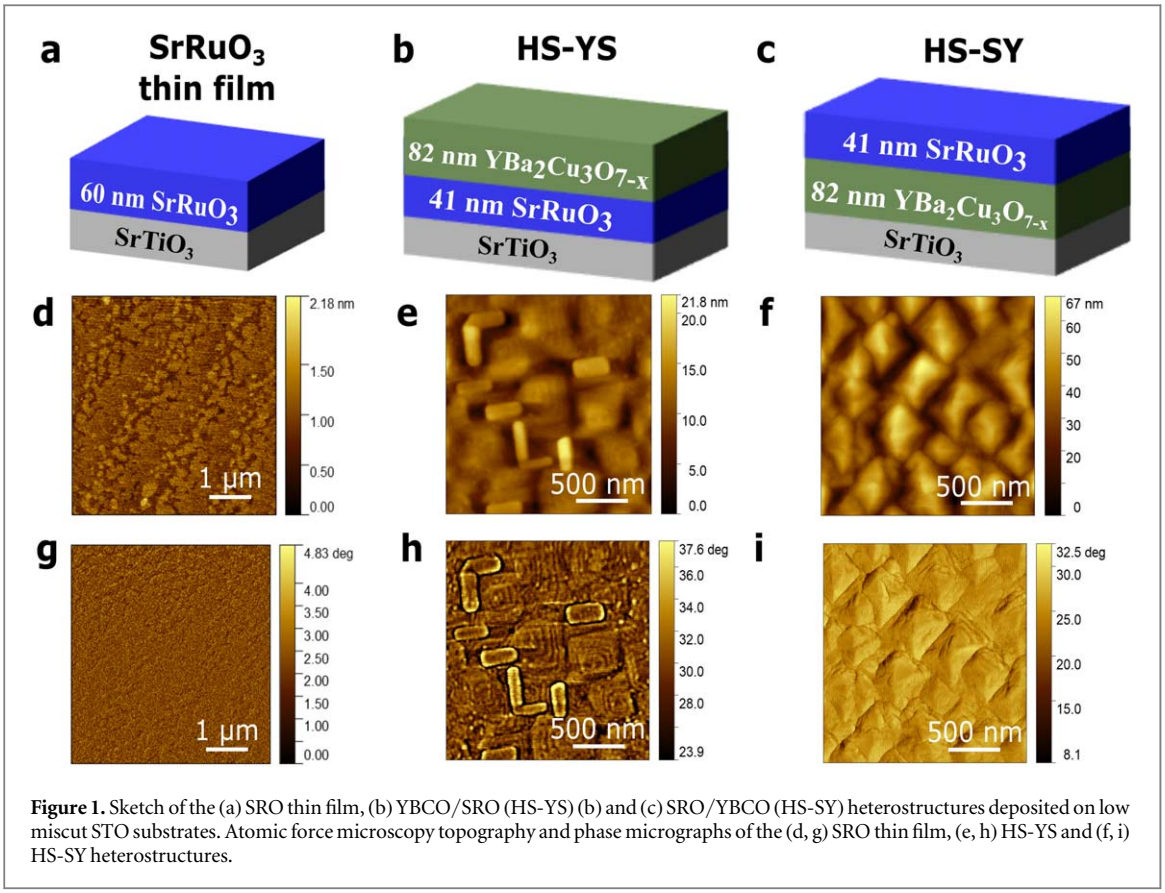

Figure 1. Sketch of the (a) SRO thin film, (b) YBCO/SRO (HS-YS) (b) and (c) SRO/YBCO (HS-SY) heterostructures deposited on low miscut STO substrates. Atomic force microscopy topography and phase micrographs of the (d, g) SRO thin film, (e, h) HS-YS and (f, i) HS-SY heterostructures.

in figure 1(g). Despite achieving a considerable degree of surface quality, the presence of small islands along the terrace edges implies a growth mode that deviates from step-flow [54–58]. Therefore, the film shows a tendency towards a step-bunching growth mode accompanied by island formation.

The morphology characterization of HS-YS is presented in the AFM micrographs shown in figures 1(e) and (h). The rectangular grains are related to the local growth of YBCO *ab*-planes oriented perpendicularly to the SRO surface (*a*-axis epitaxial growth), and the spirals are related to the growth of YBCO *ab*-planes oriented parallel to the SRO surface (*c*-axis epitaxial growth) [52, 53, 59, 60]. The local root mean square roughness σ is 2.9 nm $\pm$ 0.4 nm. The AFM topography and phase micrographs of the HS-SY, presented in figures 1(f) and (i), respectively, indicate that the SRO grew in island mode with twinning along the [110] direction. HS-SY exhibits a high local root mean square roughness ($\sigma = 6.8$ nm $\pm$ 0.4 nm) when compared to HS-YS. Such a value is expected considering that the YBCO prepared directly on STO substrates can have mixed *a*-axis and *c*-axis orientation [45, 47, 52, 53] and that YBCO thin films are usually rougher than SRO thin films, with a local roughness of $\approx$ 3 nm. Furthermore, during the growth and post-annealing process of the YBCO films, the formation of CuO and $BaCuO_3$ precipitates/nanoparticles can occur [61, 62]. These nanoparticles protrude from the film's surface, influencing the YBCO morphology. They can be seen as dots at the surface of HS-YS in the AFM micrograph shown in figure 1(h) and partially dissolved in the SRO layer deposited on YBCO layer. Therefore, the SRO layer of HS-SY was not grown on a smooth buffer layer as in the case of HS-YS, where it grew on a smooth and well-terminated surface of the SRO.

The XRD patterns of all samples are shown in figure 2. The SRO thin film exhibits long range Laue oscillations, confirming its high crystalline quality and large coherent volume ([51], figure S3). The thickness estimated by the period of the oscillations is 57 nm, which is in good agreement with the thickness obtained by XRR (60.0 nm $\pm$ 0.5 nm) ([51], figure S1). While the thickness determined by Laue oscillations corresponds to the single crystalline layer thickness, the thickness determined by reflectivity corresponds to the total layer thickness. In addition, the epitaxial growth was verified by high resolution reciprocal space mapping ([51], figure S3).

The heterostructures exhibit a high crystalline quality, as evidenced by the intensity of the crystallographic reflections. The intense (*h*00) reflections indicate that the YBCO has a greater amount of *a*-axis domains embedded in a matrix of *c*-axis domains for HS-YS than for HS-SY. CuO, $BaCuO_2$, Y_2BaCuO_5 and $YBa_3Cu_4O_x$ nanoparticles are also indexed, as indicated by the triangles in figure 2 [61, 62]. In the HS-SY XRD pattern, the YBCO reflections are slightly shifted to smaller angles, which can be related to strain. In addition, the XRD

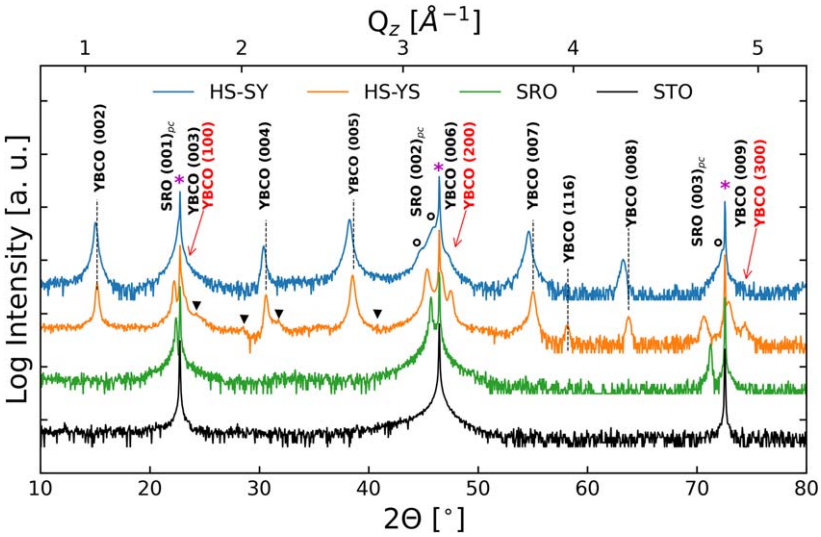

Figure 2. X-ray diffraction patterns along the surface normal of STO substrate (black), SRO thin film (green), YBCO/SRO (HS-YS) (orange) and SRO/YBCO (HS-SY) (blue) heterostructures. An STO substrate pattern is shown (black) as reference. The curves have been shifted vertically for better visibility. The asterisks point to the STO (00*l*) peaks. The triangles point to reflections from BaCu oxides precipitates embedded in the SRO layer of the HS-YS heterostructure. The empty circles indicate the formation of different SRO out-of-plane lattices parameter for the HS-SY heterostructure.

pattern of HS-SY shows broad and low-intensity SRO peaks as marked by the empty circles, indicating multiple *c*-axis orientations and non-uniform lattice parameters, suggesting an SRO layer with inferior crystalline quality in comparison to the one in HS-YS. This is expected since SRO was deposited on a relatively rough YBCO surface containing growth spirals, *a*-axis grains and possible precipitates, whereas in HS-YS, it was grown on a well-defined STO surface.

To further investigate the samples crystalline structure and, more importantly, the interface quality, an SRO (35 nm)/YBCO(20 nm)/SRO(35 nm) heterostructure was grown on an STO substrate and lamellas along the [001] and [110] crystallographic directions were prepared for characterization via transmission electron microscopy (TEM). Figure 3 shows cross-sectional images obtained along the [110] crystallographic direction. Figure 3(a) shows a wide panel of the lamella with the SRO/YBCO (top), YBCO/SRO(middle) and SRO/STO (bottom) interfaces highlighted. One can see the reduced structural quality of the SRO layer grown on the YBCO layer in comparison with the SRO layer grown on the STO substrate. The epitaxial growth of the heterostructures is confirmed in figures 3(b)–(d), given the cube-on-cube relation with considerable sharp interfaces.

Table 1 summarizes the experimentally determined values for thickness (calculated from XRR and TEM), surface (AFM) and interfacial (XRR) roughness described in this section. Table 1 also presents values of T_{Curie} and T_{c} determined from magnetization curves discussed in subsection 3.2.

3.2. Magnetic and electrical transport properties

Field cooled (FC) and electrical transport measurements of a 60 nm SRO thin film are shown in figure 4. It can be seen that although the SRO thin film has $T_{\mathrm{Curie}} = 154.7\ \mathrm{K} \pm 0.5\ \mathrm{K}$ and exhibits PMA, the saturation moment values calculated at 5 K are much lower ($\approx 0.2\ \mu_B$/Ru) compared to the bulk value ($\approx 1.6\ \mu_B$/Ru) [8, 40]. In addition, the temperature dependence of resistivity is similar to that of a semiconductor. RBS measurements ([51], figure S4) revealed that our SRO films can have $\approx 25\%$ of Ru deficiency, resulting in SRO thin films with reduced magnetization, reduced PMA and poor metallicity. This happens due to the high volatility of Ru during thin film growth [63] and the low growth rate, a characteristic of the RF sputtering method. However, even films prepared with DC sputtering present a Ru deficiency of approximately 16% [54]. This suggests that the SRO thin films may have a considerable number of defects due to Ru vacancies, which results in the observed semiconductor-like property unlike stoichiometric SRO films. Although our samples have Ru deficiency, affecting their electric and magnetic properties, PMA is present in all samples.

Zero-field cooled (ZFC) and FC measurements were performed to investigate the superconducting and ferromagnetic properties of the HS-YS and HS-SY bilayers. As a protocol, a magnet reset was initially performed on the SQUID coils to guarantee zero-field while cooling the sample down, therefore ensuring no trapped flux in the superconducting layers. After reaching 5 K, 10 Oe was applied perpendicular to the sample surface (out-of-

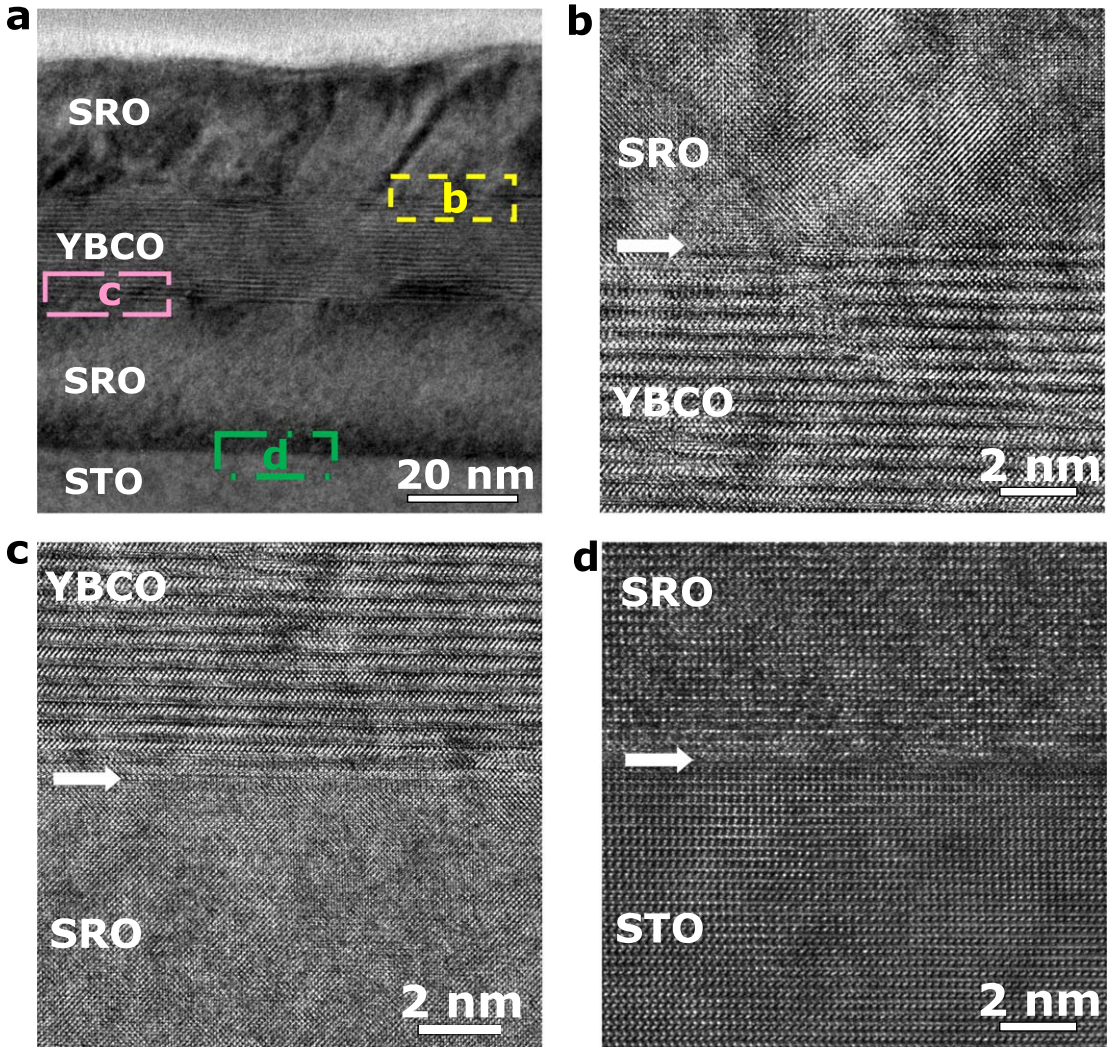

Figure 3. High resolution transmission electron microscopy images of the (a) SRO(35 nm)/YBCO(20 nm)/SRO(35 nm) heterostructure grown on a STO substrate along the [110] crystallographic direction. The respective (b) SRO/YBCO, (c) YBCO/SRO and (d) SRO/STO interfaces between the respective layers are pointed out with white arrows. Minor smearing of the images at the interface may be an artifact from sub-optimal alignment of the sample.

Table 1. Thickness by XRR (t_{XRR}) and TEM (t_{TEM}), roughness by AFM (σ_{AFM}) and XRR (σ_{XRR}), T_{Curie} and T_c calculated from magnetization measurements of the $SrRuO_3$ (SRO), $YBa_2Cu_3O_{7-x}$ (YBCO) thin films, and the heterostructures HS-YS and HS-SY, respectively.

Value	SRO	YBCO	HS-YS	HS-SY
t_{XRR} (nm)	60 ± 0.5	84.3 ± 3	—	—
t_{TEM} (nm)	—	—	40.6 ± 0.7	82.8 ± 1.9
σ_{AFM} (nm)	0.23 ± 0.01	2.5 ± 0.5	2.9 ± 0.4	6.8 ± 0.4
σ_{XRR} (nm)	1.8 ± 0.3	2.5 ± 0.1	—	—
T_{Curie} (K)	154.7 ± 0.5	—	151 ± 0.5	151 ± 0.5
T_c (K)	—	87.5 ± 0.6	87 ± 0.5	57 ± 0.5

plane, B // [001] crystallographic direction). The field direction was chosen to correspond to the magnetization easy axis of SRO. The magnetization of the samples was measured while heating up the sample to 300 K with 10 Oe applied parallel to the [001] crystallographic direction. Upon reaching 300 K, the sample was cooled down again to 5 K with 10 Oe applied parallel to the [001] crystallographic direction, while the magnetization was measured during the cooling of the samples.

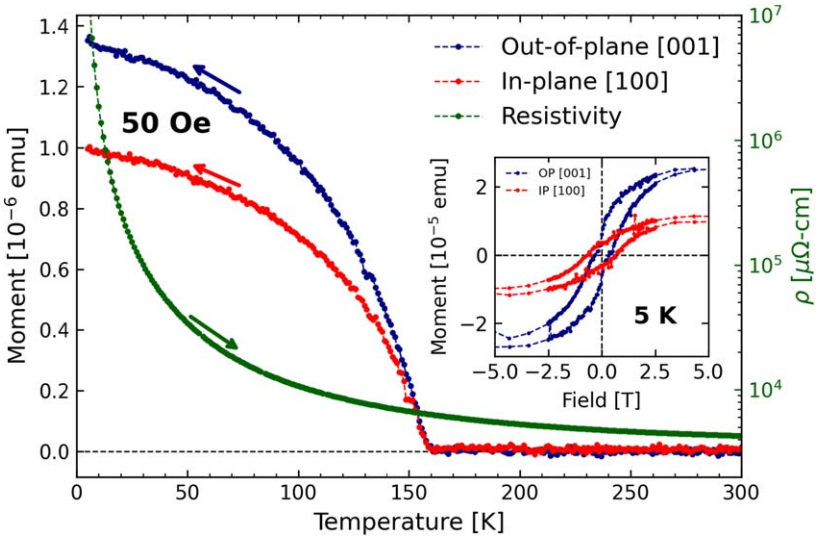

Figure 4. Field cooled magnetization acquired with a magnetic field of 50 Oe applied perpendicular (blue) and parallel (red) to sample surface and zero field electrical transport $\rho(T)$ (green) of a 60 nm SRO thin film. Magnetic hysteresis loops performed at low temperature with magnetic field applied along [001] and [100] crystallographic directions are shown in the inset.

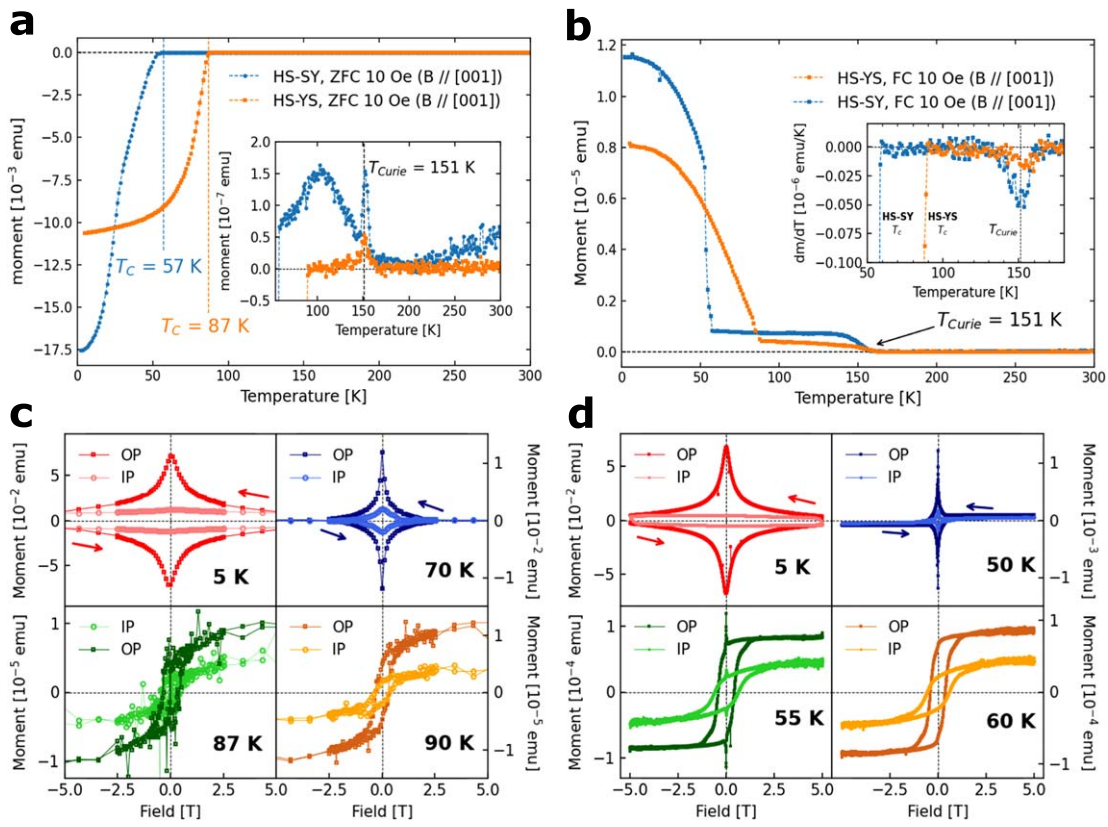

Figure 5. Zero-field cooled (a) and Field cooled (b) magnetization measurements of HS-YS and HS-SY acquired with magnetic fields of 10 Oe applied parallel to the [001] crystallographic direction, respectively. Magnetic hysteresis loops performed at low temperature and around the superconductor T_c for (c) HS-YS and (d) HS-SY.

ZFC data of HS-YS and HS-SY are shown in figure 5(a). Initially, at lower temperatures, both heterostructures exhibit a negative magnetization attributed to the diamagnetic response of the SC state of YBCO [43, 64]. As the temperature increases, the magnetization exhibits a small positive value, defining the heterostructures SC critical temperature T_c of 87 K $\pm$ 0.5 K for HS-YS and 57 K $\pm$ 0.5 K for HS-SY. The inset in figure 5(a) provides a detailed view of magnetization between the temperature range of 55 K and 300 K. Within

this range, the magnetic moment remains positive, and distinct features emerge: HS-YS displays a minimal magnetic moment, whereas HS-SY exhibits a broad maximum around 100 K, and a sharp magnetic transition is observed at 151 K for both heterostructures, which may correspond to the T_{Curie} of the SRO films. The broad hump-shaped unexpected transition observed around 100 K for HS-SY, shown in the inset of figure 5(a), may be attributed to the lattice-coherent [45] CuO and Y_2O_3 nanoparticles formed during the growth and post-annealing process of HS-SY. One can see the nanoparticles at the surface of our HS-YS sample in figure 1(h) and elsewhere [52, 53]. Yanmaz *et al* [61] reported anomalous magnetic behavior in $YBa_2Cu_3O_7$ powders coming from CuO and Y_2O_3 components. They observed a weak ferromagnetic signal at several temperatures, which is correlated with the CuO and Y_2O_3 components grinding time and nanoparticles size. We believe that CuO nanoparticles, present on the surface of the YBCO layer, were incorporated into the SRO layer during the growth of the HS-SY sample and present a plausible explanation for this observed smeared out magnetic transition.

Although some small and positive magnetization is observed above T_c in the ZFC curves, the strong diamagnetism of the superconductor hinders the study of the ferromagnetism of SRO at low temperatures. To overcome this issue, and to specifically define T_{Curie} of the SRO in these heterostructures while proving that the ferromagnetic ordering is present at low temperatures, FC measurements were performed for both heterostructures and the results are shown in figure 5(b). T_{Curie} was determined by analyzing the first derivative of the FC data, as shown in the inset of figure 5(b). Remarkably, for both samples, T_{Curie} was found to be 151 K $\pm$ 0.5 K, which corresponds to the sharp magnetic transition observed in the inset of figure 5(a). One can see that the SRO ferromagnetism is present for the entire temperature range of temperature below T_{Curie}, given the positive magnetization values at low temperatures for both samples. This confirms the coexistence of SC and FM below T_c. A small guide field (10 Oe) was sufficient to overcome the superconducting diamagnetism of YBCO because out-of-plane oriented magnetic field can penetrate through superconducting film in the form of Abrikosov vortices. Additionally, its out-of-plane orientation aligns with the easy magnetization axis of SRO, and the mixed *a*- and *c*-axis growth of YBCO disrupts the uniformity of superconducting screening along the *c*-axis. As a result, the out-of-plane diamagnetic response is weakened, potentially lowering B_{c1} and allowing magnetic flux penetration even at low magnetic fields.

Magnetic hysteresis curves taken at different temperatures are shown in figure 5(c) for HS-YS and in 5(d) for HS-SY. Measurements were carried out starting with an applied magnetic field (H_{ext}) of 5 T, then sweeping it to H_{ext} = -5 T and back to H_{ext} = 5 T again, as indicated by the arrows. In both samples, there is a change from a SC state to a FM state with increasing the temperature. From the hysteresis loops at low temperatures, we observe that both heterostructures are in a SC state, given the diamagnetic nature of the hysteresis curve, which is generally explained by the Anderson flow model [42, 65]. In addition to the Meissner effect, magnetic flux lines are trapped in defects of the sample crystal structure, near $H_{ext} = 0$ for values smaller than B_{c1} ($\approx$ 10 mT for YBCO), which results in maximum magnetization. However, as H_{ext} increases, stronger magnetic flux lines penetrate and spread in the YBCO and the magnetization decreases. The magnetization data shown in figures 5(c) and (d) exhibit characteristic behavior seen in high-T_c superconductors [66–68], indicating robust pinning effects in both heterostructures. Near T_c it is possible to detect a FM response from the shape of the hysteresis curve. This behavior becomes more pronounced when measuring at temperatures slightly below/above the heterostructure T_c, for example at 87 K for HS-YS and 55 K for HS-SY, as shown in figures 5(c) and (d), respectively. From this behavior we infer that a competition between the SC and FM states occurs. The pinning of flux lines is also confirmed, given the difference of almost three orders of magnitude in the magnetization of the heterostructures when comparing the SC and FM states [66].

Electrical transport measurements, shown in figure 6, show a drop in resistivity around the critical temperatures T_c determined from Zero-field cooling magnetization measurements. T_c values of 87.2 K $\pm$ 0.6 K for HS-YS and 57.8 K $\pm$ 0.9 K for HS-SY were obtained by taking the first derivative of $\rho(H = 0, T)$. As the transport properties of superconducting cuprates are related to hole-doping concentration [69], HS-YS is optimally doped (given the linear relation between resistivity and temperature above T_c) while HS-SY is underdoped (given the non-monotonic relation of ρ(T) above T_c). T_c values in HS-YS and HS-SY are reduced compared to our single YBCO thin films (91.1 K).

It is known that the interface quality and/or the direct contact of a SC layer with a normal metal (N)/FM layer can reduce T_c and change the width of the superconducting transition [70, 71]. Therefore, a reduction in T_c of a few Kelvins is expected for HS-YS and HS-SY, and may be due to a proximity effect, considering the presence of the FM layer in both heterostructures. This proximity effect is short-ranged, given the small coherence length values of type-II superconductors, such as YBCO. The reduction of $\approx$ 35 K in T_c for HS-SY in comparison to a purely YBCO film is not solely due to the proximity effect, but also to the sample configuration. This large reduction is explained considering that the YBCO layer is not optimally hole-doped (the oxygen transport through the SRO is hindered during the post-annealing process and therefore the YBCO layer cannot be properly oxygenated). This sample configuration prevents a rapid oxygen diffusion to the YBCO layer, thereby resulting in a YBCO film that is not optimally doped, but underdoped, and with lower T_c, as confirmed by the

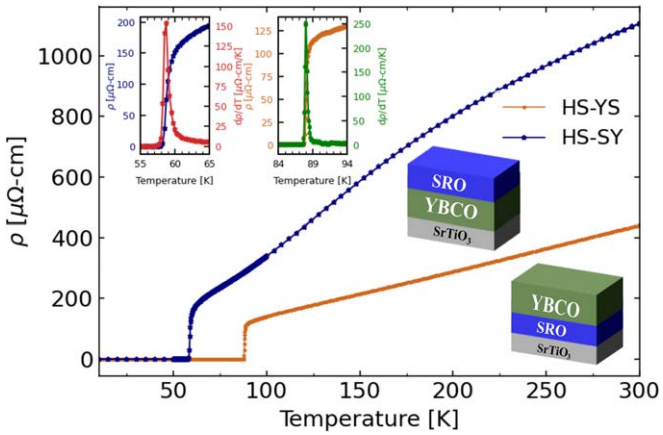

Figure 6. Zero-field $\rho(T)$ measurements of HS-YS and HS-SY heterostructures. The first derivative of $\rho(T)$ for both heterostructures is plotted in the inset.

$\rho(T)$ dependence shown in figure 6. Therefore, during the deposition of the SRO layer in HS-SY, the YBCO oxygen content changes causing the reduction in T_c, which is not recovered even after a second post-annealing process. For these reasons, HS-SY degrades faster than HS-YS, preventing a complete investigation.

3.3. Magnetotransport

Features in magnetotransport measurements of SC/FM heterostructures $\rho(H, T)$ can be robust indicators of proximity effects [10, 11, 15]. $\rho(H, T)$ was measured at selected temperatures around T_c, as shown by the colored squares in the Zero-field $\rho(T)$ curves in figure 7(a) for the HS-YS heterostructure. The measurements shown in the subsequent figures were carried out by sweeping the applied magnetic field H_{ext} from 5 T to -5 T (black curves) and then from -5 T to 5 T (colored curves). The colors correspond to the color of the squares in the figures 7(a), and thus the temperature at which the sweep was performed. H_{ext} was applied parallel (in-plane, $H_{ext,\parallel}$), figure 7(b), and perpendicular (out-of-plane, $H_{ext,\perp}$), figure 7(c), to the heterostructure surface. The in-plane and out-of-plane $\rho(H, T)$ measurements were performed with current density $\mathbf{J}\parallel H_{ext}$ and $\mathbf{J}\perp H_{ext}$, respectively. MR data for HS-SY are not presented in the current study due to technical reasons.

For temperatures above $T = 93$ K, no special features are observed in the $\rho(H, T)$ curves shown in figures 7(b)–(c) for HS-YS, and the magnetoresistance (MR) curves resembles that of YBCO thin film at these temperatures ([51], figure S5). For $T < 88$ K, the YBCO layer increasingly enters a completely SC state, as evidenced by the zero resistivity. However, a very intriguing behavior is observed at the SC onset (93 K $> T >$ 90 K) while sweeping down (black curves) and up (colored curves) H_{ext}: a crossover from a dip to a peak for $H_{ext,\parallel}$ and from a peak to a dip for $H_{ext,\perp}$ centered at 0 T. The crossover corresponds to a change in the MR signal and appears at the same temperature for H_{ext} applied in-plane and out-of-plane.

To gain more insight into the MR low field region, the $\rho(H, T)$ curves shown in figures 7(b)–(c) are plotted from -2 T to 2 T as a function of temperature in figures 7(d)–(f) for $H_{ext,\parallel}$ and figures 7(g)–(i) for $H_{ext,\perp}$. For better comparison, the plotted values of MR are normalized using the expression $\mathrm{MR}\,(\%) = \frac{100(\%) \times [\rho(H) - \rho(0)]}{\rho(0)}$. The dip (peak) observed at 91 K transforms into a peak (dip) at 89 K for $H_{ext,\parallel}$ ($H_{ext,\perp}$). Additionally, the features observed at 90 K and 89 K appear broader for $H_{ext,\parallel}$ than for $H_{ext,\perp}$, indicating a damping effect in the parallel field configuration. Although sharp peaks near zero field are not observed for 90 K and 89 K for $H_{ext,\parallel}$, the change in the MR signal is present for both field directions. The switching field, the field at which the magnetoresistance begins to change, is larger for $\rho(H, T)$ acquired with $H_{ext,\parallel}$ ($\pm$ 1 T) than $H_{ext,\perp}$ ($\pm$ 0.4 T).

Note that the observed MR features appear at switching fields that do not correspond to the coercive field of the SRO thin film. The electrical resistivity values shown in figures 7(a)–(c) are significantly lower than that of a single SRO thin film (see figure 4). Assuming the electrical resistivity of the SRO layers in HS-YS is comparable in magnitude to that of standalone SRO thin films, it can be hypothesized that the magnetoresistance observed in this heterostructure is predominantly influenced by the YBCO layer.

4. Discussion

Heterostructures of YBCO/SRO (HS-YS) and SRO/YBCO (HS-SY) have been prepared by high oxygen pressure sputtering. In both samples, the YBCO thin film exhibits local epitaxial growth of mixed *a* and *c*

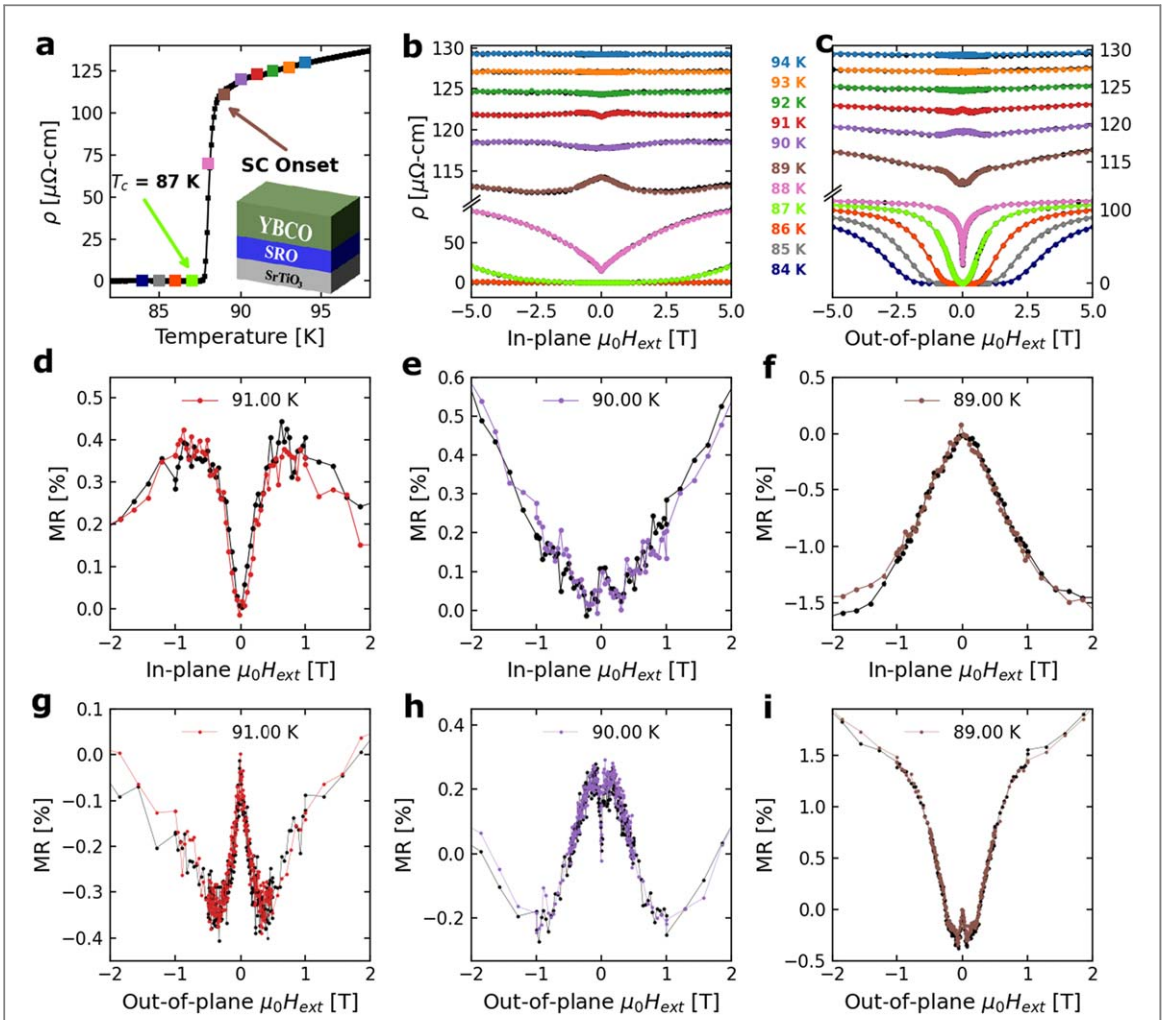

Figure 7. (a) Zero-field $\rho(T)$ curve illustrating the temperatures where $\rho(H, T)$ curves were performed with an in-plane (b) and out-of-plane (c) magnetic field measured on HS-YS heterostructure. Normalized magnetoresistance acquired with magnetic field applied in-plane for (d) 91 K, (e) 90 K and (f) 89 K. Normalized magnetoresistance acquired with magnetic field applied out-of-plane for (g) 91 K, (h) 90 K and (i) 89 K.

crystallographic domains, as shown in figures 1(e), (h) and (f), (i). In addition, the formation of CuO, $BaCuO_2$, Y_2BaCuO_5 and $YBa_3Cu_4O_x$ nanoparticles is observed during the YBCO growth and post-annealing stages, as identified by XRD and observed by AFM as small nanoscale features in the YBCO surface of HS-YS sample shown in figures 1(e), (h). These nanoparticles may have been partially dissolved within the SRO film during the growth of the HS-SY heterostructure, reflecting in its high roughness. On the other hand, prepared SRO thin films have a Ru deficiency that can reach values of 25% ([51], figure S4). As a result, the SRO thin films have reduced saturation magnetization and semiconducting behavior, seen in figure 4. This deficiency can be even more pronounced for the heterostructures, once the YBCO is prepared at a higher T_{dep} than the SRO. Nevertheless, SRO is magnetic with a T_{Curie} of 154.7 K $\pm$ 0.5 K and exhibits perpendicular magnetic anisotropy (PMA) in both heterostructures as concluded from magnetic measurements shown in figure 5.

Superconducting T_c of 87 K $\pm$ 0.5 K and 57 K $\pm$ 0.5 K are observed in Zero-field cooled magnetization and electrical transport measurements for HS-YS and HS-SY, respectively, as presented in figures 5 and 6. Both heterostructures show coexistence of SC and FM below T_c, with the easy magnetization axis lying along the out-of-plane direction. Magnetoresistance (MR) measurements were carried out around the superconducting T_c of HS-YS. We observed an anomalous MR behavior as a function of temperature and applied magnetic field direction near the onset of SC. Such a feature is not observed in pure YBCO and SRO thin films ([51], see figure S5). The MR of pure YBCO thin films is always positive and becomes infinite below T_c. SRO thin films exhibit a strong negative magnetoresistance in high fields and show the typical butterfly loop of FM materials, however, small positive MR can be found at $H_{ext} \leqslant H_c$ at low temperatures and particularly when $H_{ext} \| \mathbf{J}$. It is known that MR of SRO thin films can be anisotropic with respect to the crystalline directions rather than to the direction of the current. The anisotropic magnetoresistance can be related to an anisotropic spin-orbit interaction, therefore, suggesting the presence of weak anti-localization in SRO thin films [72–76].

We suggest that the reduction in T_c and the anomalous MR behavior observed in the YBCO/SRO heterostructure is driven by the proximity of the SC and FM layers in the heterostructures. The nature of competition between the two layers appears to be modulated by the anisotropic coherence length ξ of YBCO, which is larger along the *ab* crystallographic plane, and the uniaxial magnetocrystalline anisotropy of SRO, which has its easy axis along the $[001]_{pc}$ direction. This leads to two cases: (i) for a magnetic field applied along $[100]_{pc}$ direction, SRO magnetization lies on its hard magnetization axis and the larger magnitude of ξ_{ab} of YBCO requires a large magnetic field to show prominent features near its critical temperature T_c, thus the anomalous behavior in the MR is not strong and the peaks appear broader (as seen at 91 K) and damped/not visible (as at 90 K and 89 K), since YBCO ξ_{ab} dominates the weak hard-axis magnetization of SRO; (ii) for a magnetic field applied out-of-plane, SRO magnetization lies on its easy magnetization axis and therefore shows a higher magnetic moment in comparison to the in-plane direction. In this case, the relatively smaller ξ_c of YBCO in this direction is more sensitive to magnetic fluctuations, as observed by the sharp peaks around zero field in the MR low field region. Our experimental results point to an as yet fully unexplained and possibly novel proximity effect. Furthermore, the fact that our YBCO films show only positive magnetoresistance while the SRO films present negative magnetoresistance corroborate with the occurrence of a proximity effect.

Our MR measurements show neither the separated minima nor the sharp maxima that are indications of domain superconductivity and the generation of long-range spin-triplet components. This is evident when considering that the SC coherence length ξ of YBCO is not compatible with the characteristic length scales of the SRO magnetic domain pattern, nor does the critical field B_{c2} match the stray fields of SRO. Considering the reduced magnetization and the semiconductor properties of the SRO layer, one can argue that the YBCO/SRO interface can be semiconducting or insulating as well as magnetically dead/depleted. Indeed there is an intriguing similarity between the shape of $\rho(H, T)$ as a function of the applied magnetic field direction at temperatures around the SC onset and the shape of the quantum corrections to conductivity, more precisely weak localization and weak anti-localization, commonly observed in semiconductor and insulating systems [1, 77]. However, quantum corrections to conductivity are a true low temperature phenomena and are unlikely to explain our results. The formation of a magnetic dead layer should be further investigated with stoichiometric thinner samples, which would increase the sensitivity to the interface properties. The observed complex behavior around T_c could also be correlated with the interplay between the presence of defects, orbital reconstruction due to strain in the interfaces, strong spin–orbit coupling and potential charge transfer between the layers. The coupling between these factors should be further elucidated by carrying out experimental investigations supported by first principle calculations.

5. Conclusion

Epitaxial samples based on the high-T_c SC and FM with PMA were prepared with the aim to characterize proximity effects at the interface between high-T_c SC and FM layers and to understand the nature of such proximity effects. Due to compatible crystal structures and the presence of PMA, heterostructures of SRO and YBCO prepared on STO substrates were selected and prepared in good quality by HOPS. Due to incompatible characteristic length scales between the SRO magnetic domain periodicity and the YBCO coherence length ξ on the one hand, and the incompatible sizes of the magnetic stray field of the SRO domain structure and the critical field B_{c2} of YBCO on the other hand, the proximity effects observed in heterostructures of FM and conventional SC, such as domain superconductivity and the generation of long-range spin-triplet components do not occur in the investigated heterostructures. We propose, as alternative, a proximity effect that is modulated by the competition between the anisotropic coherence length in YBCO and the uniaxial magnetocrystalline anisotropy of SRO. The findings inspire further theoretical and experimental explorations in fundamental science and technological applications, especially in the field of quantum materials.

Acknowledgments

The authors gratefully acknowledge the technical assistance of F Gossen, L Kibkalo and B Schmitz. The authors acknowledge U Poppe, A Stellhorn, K Friese and M Radovic for the discussions. This work was sponsored by the Tasso Springer Fellowship provided by JCNS.

Conflict of interest

The authors have no conflicts to declare.

Data availability statement

The data cannot be made publicly available upon publication because no suitable repository exists for hosting data in this field of study. The data that support the findings of this study are available upon reasonable request from the authors.

Author contributions

V A de Oliveira Lima: conceptualization, sample preparation, AFM, magnetization, transport and magnetotransport measurements, data curation, investigation, writing - original draft, review & editing. **M I Faley:** conceptualization, sample preparation, TEM measurements, investigation. **O Concepción:** XRD, XRR and RBS measurements. **S Nandi:** supervision, investigation, writing - review & editing. **P Prakash:** writing - review & editing. **M H Hamed:** writing - review. **E Kentzinger:** conceptualization, supervision, writing - review. **T Brückel:** conceptualization, investigation, writing - review & editing. **C Bednarski-Meinke:** supervision, writing - review & editing.

ORCID iDs

V A de Oliveira Lima https://orcid.org/0000-0002-9589-3600
M I Faley https://orcid.org/0000-0003-2768-2796
O Concepción https://orcid.org/0000-0001-8197-7523
S Nandi https://orcid.org/0000-0002-7411-3652
M H Hamed https://orcid.org/0000-0001-8165-1216
E Kentzinger https://orcid.org/0000-0002-5348-7591
T Brückel https://orcid.org/0000-0003-1378-0416
C Bednarski-Meinke https://orcid.org/0000-0003-1509-1876

References

[1] Bluhm H, Brückel T, Morgenstern M, Plessen G and Stampfer C 2019 *Electrons in Solids: Mesoscopics, Photonics, Quantum Computing, Correlations, Topology* ed C Enss (Walter de Gruyter GmbH & Co KG)
[2] Cai R, Žutić I and Han W 2023 Superconductor/ferromagnet heterostructures: a platform for superconducting spintronics and quantum computation *Adv Quantum Technol.* **6** 2200080
[3] Uribe-Laverde M A *et al* 2013 Depth profile of the ferromagnetic order in a $YBa_2Cu_3O_7/La_{2/3}Ca_{1/3}MnO_3$ superlattice on a LSAT substrate: a polarized neutron reflectometry study *Phys. Rev. Bok.* **87** 115105
[4] Buzdin A I and Mel'nikov A 2003 Domain wall superconductivity in ferromagnetic superconductors *Phys. Rev. B* **67** 020503
[5] Linder J and Robinson J W 2015 Superconducting spintronics *Nat. Phys.* **11** 307–15
[6] Kadin A 1990 Duality and fluxonics in superconducting devices *J. Appl. Phys.* **68** 5741–9
[7] Dobrovolskiy O V and Chumak A V 2022 Nonreciprocal magnon fluxonics upon ferromagnet/superconductor hybrids *J Magn Magn Mater* **543** 168633
[8] Cuoco M and Di Bernardo A 2022 Materials challenges for $SrRuO_3$: from conventional to quantum electronics *APL Mater* **10**
[9] Stellhorn A 2021 Interplay of proximity effects in superconductor/ferromagnet heterostructures *PhD thesis.* RWTH Aachen University
[10] Stellhorn A *et al* 2020 Tailoring superconducting states in superconductor-ferromagnet hybrids *New. J. Phys.* **22** 093001
[11] Yang Z, Lange M, Volodin A, Szymczak R and Moshchalkov V V 2004 Domain-wall superconductivity in superconductor-ferromagnet hybrids *Nat. Mater.* **3** 793–8
[12] Eschrig M 2011 Spin-polarized supercurrents for spintronics *Phys Today* **64** 43–9
[13] Aladyshkin A Y, Buzdin A, Fraerman A, Mel'nikov A, Ryzhov D and Sokolov A 2003 Domain-wall superconductivity in hybrid superconductor-ferromagnet structures *Phys. Rev. B* **68** 184508
[14] Zdravkov V I *et al* 2013 Experimental observation of the triplet spin-valve effect in a superconductor-ferromagnet heterostructure *Phys. Rev. B* **87** 144507
[15] Gu Y, Halász G B, Robinson J and Blamire M 2015 Large superconducting spin valve effect and ultrasmall exchange splitting in epitaxial rare-earth-niobium trilayers *Phys. Rev. Lett.* **115** 067201
[16] Gu J, You C Y, Jiang J, Pearson J, Bazaliy Y B and Bader S 2002 Magnetization-orientation dependence of the superconducting transition temperature in the ferromagnet-superconductor-ferromagnet system: CuNi/Nb/CuNi *Phys. Rev. Lett.* **89** 267001
[17] Prajapat C *et al* 2018 Proximity effects across oxide-interfaces of superconductor-insulator-ferromagnet hybrid heterostructure *Sci. Rep.* **8** 3732
[18] Di Bernardo A *et al* 2019 Nodal superconducting exchange coupling *Nat Mater* **18** 1194–200
[19] Chakhalian J *et al* 2006 Magnetism at the interface between ferromagnetic and superconducting oxides *Nat. Phys.* **2** 244–8
[20] Stahn J *et al* 2005 Magnetic proximity effect in perovskite superconductor/ferromagnet multilayers *Phys. Rev. B* **71** 140509
[21] Pena V *et al* 2005 Giant magnetoresistance in ferromagnet/superconductor superlattices *Phys. Rev. Lett.* **94** 057002
[22] Sanchez-Manzano D *et al* 2024 Long-range superconducting proximity effect in $YBa_2Cu_3O_7/La_{0.7}Ca_{0.3}MnO_3$ weak-link arrays *Appl. Phys. Lett.* **124** 222603
[23] Chou H *et al* 2024 Controllable spin-triplet superconductivity states and enhanced non-dissipation spin-polarized supercurrents in $YBa_2Cu_3O_7/La_{0.67}Sr_{0.33}MnO_3$ interfaces *Appl. Surf. Sci.* **644** 158739

[24] Khaydukov Y N *et al* 2014 Evidence for spin-triplet superconducting correlations in metal-oxide heterostructures with noncollinear magnetization *Phys. Rev. B* **90** 035130
[25] Ovsyannikov G *et al* 2016 Magnetic proximity effect at the interface between a cuprate superconductor and an oxide spin valve *JETP* **122** 738–47
[26] Ovsyannikov G, Constantinian K, Demidov V and Khaydukov Y N 2016 Magnetic proximity effect and superconducting triplet correlations at the cuprate superconductor and oxide spin valve interface *Low Temp. Phys.* **42** 873–83
[27] Boschker H *et al* 2019 Ferromagnetism and conductivity in atomically thin $SrRuO_3$ *Phys. Rev. X* **9** 011027
[28] Contreras J R *et al* 2005 Improved $PbZr_{0.52}Ti_{0.48}O_3$ film quality on $SrRuO_3/SrTiO_3$ substrates *J Cryst Growth* **277** 210–7
[29] Wakabayashi Y K, Kaneta-Takada S, Krockenberger Y, Taniyasu Y and Yamamoto H 2021 Wide-range epitaxial strain control of electrical and magnetic properties in high-quality $SrRuO_3$ films *ACS Appl Electron Mater* **3** 2712–9
[30] Wakabayashi Y K *et al* 2021 Single-domain perpendicular magnetization induced by the coherent O 2*p*-Ru 4*d* hybridized state in an ultra-high-quality $SrRuO_3$ film *Phys. Rev. Mater* **5** 124403
[31] Wakabayashi Y K, Otsuka T, Krockenberger Y, Sawada H, Taniyasu Y and Yamamoto H 2019 Machine-learning-assisted thin-film growth: Bayesian optimization in molecular beam epitaxy of $SrRuO_3$ thin films *APL Mater* **7**
[32] Bern F, Ziese M, Setzer A, Pippel E, Hesse D and Vrejoiu I 2013 Structural, magnetic and electrical properties of $SrRuO_3$ films and $SrRuO_3/SrTiO_3$ superlattices *J. Condens. Matter. Phys.* **25** 496003
[33] Kaneta-Takada S *et al* 2023 Scattering-dependent transport of $SrRuO_3$ films: from Weyl fermion transport to hump-like Hall effect anomaly *Phys. Rev. Mater* **7** 054406
[34] Takiguchi K *et al* 2020 Quantum transport evidence of Weyl fermions in an epitaxial ferromagnetic oxide *Nat. Commun.* **11** 4969
[35] Gu Y *et al* 2022 An overview of $SrRuO_3$-based heterostructures for spintronic and topological phenomena *J. Phys. D: Appl. Phys.* **55** 233001
[36] Marshall A *et al* 1999 Lorentz transmission electron microscope study of ferromagnetic domain walls in $SrRuO_3$: statics, dynamics, and crystal structure correlation *J. Appl. Phys.* **85** 4131–40
[37] Asulin I, Yuli O, Koren G and Millo O 2006 Evidence for crossed Andreev reflections in bilayers of (100) $YBa_2Cu_3O_{7-\delta}$ and the itinerant ferromagnet $SrRuO_3$ *Phys. Rev. B* **74** 092501
[38] Hoppler J *et al* 2008 X-ray study of structural domains in the near-surface region of $SrTiO_3$ substrates with $Y_{0.6}Pr_{0.4}Ba_2Cu_3O_7/La_{2/3}Ca_{1/3}MnO_3$ superlattices grown on top *Phys. Rev. B* **78** 134111
[39] Lytle F W 1964 X-ray diffractometry of low-temperature phase transformations in strontium titanate *J. Appl. Phys.* **35** 2212–5
[40] Koster G *et al* 2012 Structure, physical properties, and applications of $SrRuO_3$ thin films *Rev. Mod. Phys.* **84** 253–98
[41] Contreras JR. 2003 Ferroelectric Tunnel Junctions. *PhD thesis.* University of Cologne.
[42] Cardwell D A, Larbalestier D C and Braginski A 2022 *Handbook of Superconductivity: Fundamentals and Materials, Volume One* vol. 1. (CRC Press)
[43] Habermeier H, Albrecht J and Soltan S 2004 The enhancement of flux-line pinning in all-oxide superconductor/ferromagnet heterostructures *Supercond. Sci. Technol.* **17** S140
[44] Sanchez F, Ocal C and Fontcuberta J 2014 Tailored surfaces of perovskite oxide substrates for conducted growth of thin films *Chem. Soc. Rev.* **43** 2272–85
[45] Poppe U *et al* 1992 Low-resistivity epitaxial $YBa_2Cu_3O_7$ thin films with improved microstructure and reduced microwave losses *J. Appl. Phys.* **71** 5572–8
[46] Jia C, Contreras J R, Poppe U, Kohlstedt H, Waser R and Urban K 2002 Lattice strain and lattice expansion of the SrRuO3 layers in $SrRuO_3/PbZr_{0.52}Ti_{0.48}O_3/SrRuO_3$ multilayer thin films *J. Appl. Phys.* **92** 101–5
[47] Faley M I 2011 Epitaxial oxide heterostructures for ultimate high-T_c quantum interferometers *Applications of High-T_c Superconductivity* (InTech)
[48] Vassenden F, Linker G and Geerk J 1991 Growth direction control YBCO thin films *Phys. C: Supercond. Appl.* **175** 566–72
[49] Feenstra R, Lindemer T, Budai J and Galloway M 1991 Effect of oxygen pressure on the synthesis of $YBa_2Cu_3O_{7-x}$ thin films by post-deposition annealing *J. Appl. Phys.* **69** 6569–85
[50] Jorgensen J *et al* 1987 Oxygen ordering and the orthorhombic-to-tetragonal phase transition in $YBa_2Cu_3O_{7-x}$ *Phys. Rev. B* **36** 3608
[51] See Supplemental Material at https://doi.org/10.1088/1402-4896/ade7f7 for more information. de Oliveira Lima V A *et al* 2025
[52] Faley M, Jia C, Houben L, Meertens D, Poppe U and Urban K 2006 Meandering of the grain boundary and d-wave effects in high-T_c bicrystal josephson junctions *Supercond. Sci. Technol.* **19** S195
[53] Faley M, Meertens D, Poppe U and Dunin-Borkowski R 2013 Graphoepitaxial Josephson junctions and DC SQUIDs *IEEE 14th International Superconductive Electronics Conference (ISEC)* (IEEE) 2013, 1–3
[54] Mlynarczyk M *et al* 2007 Surface layer of $SrRuO_3$ epitaxial thin films under oxidizing and reducing conditions *J. Appl. Phys.* **101** 023701
[55] Hong W *et al* 2005 Persistent step-flow growth of strained films on vicinal substrates *Phys. Rev. Lett.* **95** 095501
[56] Sánchez F, Rigato F, Bachelet R and Fontcuberta J 2008 Formation of step bunching in the epitaxial growth of $SrRuO_3$ thin films *J Cryst Growth* **310** 3348–50
[57] Herranz G *et al* 2003 Impact of microstructure on transport properties of nanometric epitaxial $SrRuO_3$ films *Appl. Phys. Lett.* **82** 85–7
[58] Rao R A, Gan Q and Eom C B 1997 Growth mechanisms of epitaxial metallic oxide $SrRuO_3$ thin films studied by scanning tunneling microscopy *Appl. Phys. Lett.* **71** 1171–3
[59] Suyolcu Y E *et al* 2021 *a*-axis $YBa_2Cu_3O_{7-x}/PrBa_2Cu_3O_{7-x}/YBa_2Cu_3O_{7-x}$ trilayers with subnanometer rms roughness *APL Mater* **9** 021117
[60] Liu L, Zhao Z, Liu H and Li Y 2010 Effect of deposition temperature on the epitaxial growth of YBCO thin films on RABiTS substrates by pulsed laser deposition method *IEEE Trans Appl Supercond* **20** 1553–6
[61] Yanmaz E, Basoglu M and Grovenor C 2009 Anomalous ferromagnetic behaviour of Y_2O_3 and CuO nanoparticles in $YBa_2Cu_3O_y$ superconductor *Phys Status Solidi A* **206** 2844–50
[62] Kim Y *et al* 2006 CuO formation control as a function of mixed ratio of Cu-free powders in the synthesis of YBCO superconductors on Cu substrates *J Electroceram* **17** 1063–7
[63] Hölgye Z and Křivánek M 1978 On the volatility of ruthenium *J Radioanal Nucl. Chem.* **42** 133–41
[64] Soltan S, Albrecht J and Habermeier H U 2004 Ferromagnetic/superconducting bilayer structure: a model system for spin diffusion length estimation *Phys. Rev. B* **70** 144517
[65] Anderson P W and Kim Y 1964 Hard superconductivity: theory of the motion of Abrikosov flux lines *Rev. Mod. Phys.* **36** 39
[66] Albrecht J, Soltan S and Habermeier H U 2005 Magnetic pinning of flux lines in heterostructures of cuprates and manganites *Phys. Rev. B* **72** 092502

[67] Petrisor T et al 2012 Magnetic pinning effects of epitaxial $La_xSr_{1-x}MnO_3$ nanostructured thin films on $YBa_2Cu_3O_{7-\delta}$ layers J. Appl. Phys. 112
[68] Jha A K, Khare N and Pinto R 2014 Influence of interfacial LSMO nanoparticles/layer on the vortex pinning properties of YBCO thin film J Supercond Nov Magn 27 1021–6
[69] Blügel S, Brückel T, Waser R and Schneider C M 2010 Electronic Oxides - Correlation Phenomena, Exotic Phases and Novel Functionalities: Volume 41 of Lecture manuscripts of the Spring School of the Institute of Solid State Research vol 41 (Forschungszentrum, Zentralbibliothek)
[70] Aristomenopoulou E, Zeibekis M and Stamopoulos D 2016 Optimizing the magnitude of the magnetoresistance observed in ferromagnet/superconductor/ferromagnet trilayers: a formula to combine all involved parameters J. Appl. Phys. 119 093904
[71] Martinis J M, Hilton G C, Irwin K D and Wollman D A 2000 Calculation of T_c in a normal-superconductor bilayer using the microscopic-based Usadel theory Nucl Instrum Methods Phys Res A: Accel Spectrom Detect Assoc Equip 444 23–7
[72] Kacedon D, Rao R and Eom C 1997 Magnetoresistance of epitaxial thin films of ferromagnetic metallic oxide $SrRuO_3$ with different domain structures Appl. Phys. Lett. 71 1724–6
[73] Gausepohl S, Lee M, Char K, Rao R and Eom C 1995 Magnetoresistance properties of thin films of the metallic oxide ferromagnet $SrRuO_3$ Phys. Rev. B 52 3459
[74] Shen X, Qiu X, Su D, Zhou S, Li A and Wu D 2015 Thickness-dependent metal-insulator transition in epitaxial $SrRuO_3$ ultrathin films J. Appl. Phys. 117 015307
[75] Gunnarsson R 2012 Anisotropic spin-orbit interaction revealed by in-plane magnetoresistance in single-oriented $SrRuO_3$ thin films Phys. Rev. B 85 235409
[76] Rao R, Kacedon D and Eom C 1998 Anisotropic magnetotransport properties of epitaxial thin films of conductive ferromagnetic oxide $SrRuO_3$ J. Appl. Phys. 83 6995–7
[77] Schäpers T 2021 Semiconductor Spintronics. ed T Schäpers (Walter de Gruyter GmbH & Co KG)